

High-resolution observations with ARTEMIS-JLS and the NRH

III. Spectroscopy and imaging of fiber bursts^{*}

C. E. Alissandrakis (K. E. Αλυσσανδράκης)¹, C. Bouratzis (K. Μπουρατζής)², and A. Hillaris (A. Χείλαρης)²

¹ Department of Physics, University of Ioannina, 45110 Ioannina, Greece
e-mail: calissan@cc.uoi.gr

² Department of Physics, University of Athens, 15783 Athens, Greece

Received 5 April 2019 / Accepted 4 June 2019

ABSTRACT

Aims. We study the characteristics of intermediate drift bursts (fibers) embedded in a large type-IV event.

Methods. We used high-sensitivity, low-noise dynamic spectra obtained with the acousto-optic analyzer (SAO) of the ARTEMIS-JLS solar radiospectrograph, in conjunction with high time-resolution images from the Nançay radioheliograph (NRH) and extreme ultraviolet (EUV) images from the Transition Region and Coronal Explorer (TRACE) to study fiber bursts during the large solar event of July 14, 2000. We computed both 2D and 1D images and applied high pass time filtering to the images and the dynamic spectrum in order to enhance the fiber-associated emission. For the study of the background continuum emission we used images averaged over several seconds.

Results. Practically all fibers visible in the SAO dynamic spectra are identifiable in the NRH images. Fibers were first detected after the primary energy release in a moving type-IV event, probably associated with the rapid eastward expansion of the flare and the post-flare loop arcade. We found that fibers appeared as a modulation of the continuum intensity with a root mean square value of the order of 10%. Both the fibers and the continuum were strongly circularly polarized in the ordinary mode sense, indicating plasma emission at the fundamental. We detected a number of discrete fiber emission sources along two parallel stripes of ~300 Mm in length, apparently segments of large-scale loops encompassing both the EUV loops and the CME-associated flux rope. We found cases of multiple fiber emissions appearing at slightly different positions and times; their consecutive appearance can give the impression of apparent motion with supra-luminal velocities. Images of individual fibers were very similar at 432.0 and 327.0 MHz. From the position shift of the sources and the time delays at low and high frequencies, we estimated the exciter speed and the frequency scale length along the loops for a well-observed group of fibers; we obtained consistent values from imaging and spectral data, supporting the whistler origin of the fiber emission. Finally we found that fibers in emission and fibers in absorption are very similar, confirming that they are manifestations of the same wave train.

Key words. Sun: radio radiation – Sun: activity – Sun: flares – Sun: corona – Sun: magnetic fields

1. Introduction

Fibers are solar radio bursts with intermediate frequency drift (i.e., between the slow drifting type-II bursts and the fast drifting type-III bursts); they are observed in groups at decimetric and lower frequencies, embedded in type-IV burst continua (Young et al. 1961; Elgarøy 1972; Slottje 1972, 1981; Fomichev & Chertok 1978). In addition to their filamentary shape in dynamic spectra, another important characteristic is that they appear in the form of absorption and emission ridges, the absorption having a slightly lower frequency than the emission.

Intermediate-drift bursts are believed to be signatures of an exciter moving along post-flare magnetic loops. The exciter is most likely a train of whistler waves, radiating through their interaction with Langmuir waves (Kuijpers 1972, 1975, 1980). According to this interpretation, the emission is enhanced at $\omega_{pe} + \omega_w$ and reduced at ω_{pe} where ω_w is the whistler frequency and ω_{pe} the plasma frequency. The frequency range of the emission is limited by the condition $0.25 \leq \omega_w/\omega_{ce} \leq 0.5$, where ω_{ce} is the electron cyclotron frequency; the first part

of this relation is the necessary condition for the development of the instability and the second part is necessary for strong cyclotron damping. Alternative interpretations involve Alfvén–Langmuir wave interaction (Bernold & Treumann 1983), a combination of Alfvén waves and an electron cyclotron maser (Benz & Mann 1998), or modulation of the background type-IV continuum by fast magneto-acoustic wave trains (Kuznetsov 2006; Karlický et al. 2013; Zlobec & Karlický 2014). Whatever their origin, the intermediate-drift bursts qualify as coronal magnetic field diagnostics (see Aurass et al. 2005; Rausche et al. 2007, 2008; Bouratzis et al. 2019).

A combined analysis of dynamic spectra and images was performed by Aurass et al. (2005), who used 2D positions from the Nançay Radioheliograph together with potential extrapolations of the photospheric magnetic field and an $a \times$ Newkirk density model to identify the magnetic loops in which fiber bursts occurred. Their best fit was for $a = 3.5$ and they deduced field strengths from 6–14 G at 410 MHz (height of 20 Mm) to 3 G higher up at 100 Mm (236 MHz). A similar analysis was performed by Rausche et al. (2007). Recently, Wang et al. (2017) studied three groups of fiber bursts in the 1–2 GHz range; they used dynamic imaging spectroscopy with the Karl G. Jansky Very Large Array (VLA) which allowed the reconstruction of

^{*} Movies associated to Figs. 2, 7, and 10 are available at <https://www.aanda.org>

spatially resolved fiber trajectories. A comparison of their results with theoretical models favors the whistler wave model and points to the origin of the fiber bursts at or near the footpoints of coronal loops.

In a recent study (Bouratzis et al. 2019; hereafter Paper I) we performed an extensive analysis of a large number of fibers embedded in sixteen type-IV bursts observed with the high-sensitivity, 10 ms resolution receiver of the ARTEMIS-/Jean-Louis Steinberd (JLS) radio spectrograph. We distinguished six morphological groups of fibers and measured their duration, their bandwidth, and their drift rate as a function of time. We found that the whistler hypothesis leads to reasonable magnetic field values, while the Alfvén origin required too high a magnetic field; we derived an average magnetic field of 4.4 G and an average frequency scale length along the loop of 220 Mm.

In this work we extend the work presented in Paper I by using combined ARTEMIS-JLS and Nançay Radioheliograph (NRH) to study fibers during the flare of July 14, 2000. In Sect. 2 we present the observations and in Sect. 3 our results. We conclude with a discussion in Sect. 4.

2. Observations and their analysis

The observations with ARTEMIS-JLS (Caroubalos et al. 2001a) and their analysis were described in detail in Paper I. Here we only mention that the fibers were observed with the acousto-optic analyzer (SAO) in the frequency range of 265–470 MHz with a spectral sampling of 1.4 MHz and a temporal resolution of 10 ms. For an overview of the event we used data from the sweep-frequency Global Spectral Analyser (ASG), which operated in the 100–700 MHz range with a time resolution of 100 ms.

The Nançay Radioheliograph (Kerdraon & Delouis 1997) is a synthesis instrument that provides 2D images of the Sun with sub-second time resolution. For the event that we study here, the NRH provided data at five frequencies (164.0, 236.6, 327.0, 410.5 and 432.0 MHz) with a cadence of 125 ms. All five frequencies are within the spectral range of the ASG, while the last three are also within the range of the SAO.

From the original NRH visibilities, we computed 2D images with a resolution of 1.04' by 1.52' at 432 MHz. In a previous work on spike bursts (Bouratzis et al. 2016) we also computed 1D images using visibilities from the east-west (EW) and north-south (NS) arrays only; this improved the resolution by a factor of two, due to the fact that the extension antennas make a very small contribution to the 2D images. In the present case these 1D images were relatively noisy, whereas the fiber sources were well resolved and thus we preferred to compute 1D images by integrating the 2D images along the EW and NS directions. This gave us a less noisy and more robust result; no detailed self-calibration was necessary, but we did delete some defective baselines.

3. Results

3.1. Overview of the event of July 14, 2000

This is a famous event described by many authors (e.g., Klein et al. 2001; Masuda et al. 2001; Wang et al. 2001). ARTEMIS data were presented by Caroubalos et al. (2001b); see also Fig. 17 of Bouratzis et al. (2015). It was a complex event that occurred in active region 9077 and was associated to an X5.7 flare, starting at 10:03 UT near the center of the disk, and to a halo coronal mass ejection (CME). The flare was relatively extended in longitude (from $\sim 6^\circ$ East to $\sim 8^\circ$ West, latitude

$\sim 16^\circ$), with spectacular loops recorded at 195 Å by the Transition Region and Coronal Explorer (TRACE).

In the early phase of the event, which included the filament activation and the CME onset, the energy release was limited in the west part of the active region (Klein et al. 2001; Caroubalos et al. 2001b). The expansion of the rising filament was also directed west of the flare, and so was the bulk of the CME, with a measured position angle of 273° . Near the hard X-ray (HXR) peak at 10:26:45 UT, the flare emission expanded rapidly towards the east part of the active region and post-flare loops formed all along the neutral line.

The metric emission (Fig. 1) was dominated by a drifting continuum that started after the GOES and HXR peaks around 10:27 UT and lasted up to about 10:41 UT in the frequency range 200–450 MHz. We also have a lower intensity broadband continuum throughout the event, numerous type-III events and a faint type-II event. The continuum was rich in embedded pulsations, spikes, fibers, and zebra patterns. Fiber bursts appeared around 10:33 UT and lasted until about 11:25 (Table 2 of Bouratzis et al. 2015), often mixed with pulsations and other broadband structures (see Figs. 6–7 in Caroubalos et al. 2001b). Their bulk parameters during the drifting continuum are given in entry 11 of Table A.1 of Paper I and in entry 12 for the time interval after that.

Although some strong fibers are also visible in the ASG spectra, none were detected at the NRH frequency of 236 MHz; we therefore limited our comparative study to the three NRH frequencies that fall within the SAO range (327.0 MHz, 410.5 MHz and 432.0 MHz). We selected two time intervals of 45 s each, in which fiber bursts were relatively uncontaminated by other emissions; these are marked by vertical lines in the dynamic spectrum of Fig. 1. The first interval, from 10:38:55 to 10:39:40 UT is near the end of the drifting continuum emission and the second interval, from 11:00:05 to 11:00:50 UT, is well after that, when the continuum emission was relatively weak.

3.2. Evolution of the continuum source

Before we proceed with the fibers, it is interesting to discuss the evolution of the continuum source. For this purpose we use NRH images with a 30 s time integration. We note that the modulation of the intensity due to the fibers was small, $\sim 10\%$ in rms, and therefore the 30 s average images are representative of the background continuum. Figure 2 and the associated Movie 1 show the evolution of the radio sources at the five NRH frequencies, together with the ASG dynamic spectrum for reference. In order to compensate for the strong intensity variability, we normalized each NRH image by its maximum value.

During the early phase of the event, most of the metric emission came from the NW quadrant of the solar disk, apparently associated with the primary energy release and the beginning of the halo CME, as discussed in the previous section and described by Klein et al. (2001) and Caroubalos et al. (2001b). The movie frame of Fig. 2 shows emission that appeared NE of the flare (eastern source in Klein et al. 2001) from around 10:27 UT at high frequencies. From 10:34 UT this source dominated the drifting continuum and the entire dynamic spectrum above 164.0 MHz, while from 10:43 UT it was the only source at 164.0 MHz as well. Most importantly for us here, it was the source of the first fibers.

From about 10:33 UT, this source displayed a clear rectilinear motion to the NE at all frequencies except for 164 MHz. The motion is clearly visible in Movie 1; at the high NRH frequencies it lasted until 10:37 UT, and until 10:39 UT at 236.6 MHz.

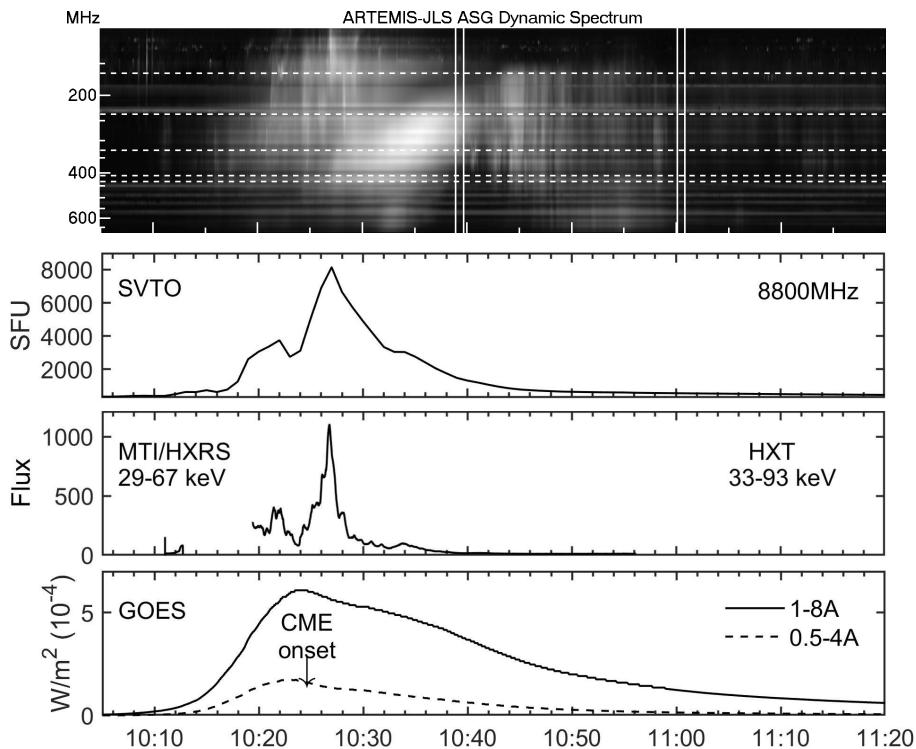


Fig. 1. Dynamic spectrum of the event of July 14, 2000, recorded by the ARTEMIS-JLS sweep frequency receiver, ASG, in the 100–670 MHz range. Dashed horizontal lines mark the NRH frequencies, vertical lines the two selected intervals of fiber emissions. The bottom plots show time curves of microwave emission at 2695 MHz from San Vito, 33–93 keV hard X-rays from the Hard X-ray Spectrometer (HXRS) on board the Multi-Spectral Thermal Imager (MTI) and the Hard X-ray Telescope (HXT) on board Yohkoh, and soft X-rays from GOES.

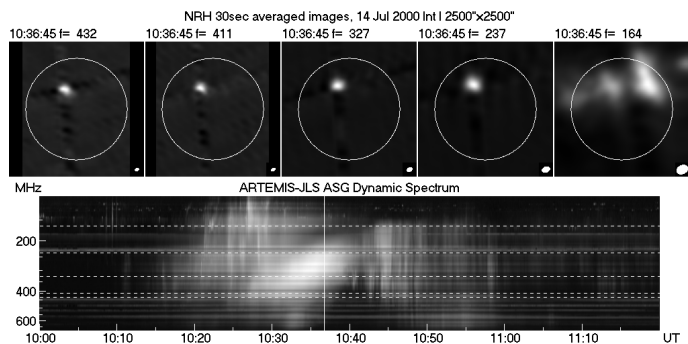


Fig. 2. Frame from *Movie 1*, showing NRH images in Stokes *I* at all five frequencies. The images are averaged over 30 s and have been normalized so that the minimum intensity of each image is black and the peak intensity is white. The white circles mark the photospheric limb. The NRH beam is drawn in the lower right corner of each frame. The bottom panel shows the ASG dynamic spectrum, with the vertical white line marking the time of the images and the dashed horizontal lines marking the NRH frequencies.

Although after that it is difficult to follow the motion of the continuum source due to the presence of broadband structures (Fig. 1), there was a development of multiple components and a net displacement to the east and south, indicating a shift of the emission source lower in the corona. At 164 MHz which, as noted above, was outside the drifting continuum, the emission did not follow the same evolution.

Figure 3 shows the trajectories of the source during the upward rectilinear motion, overplotted on an EIT image at 195 Å; although the flare image is saturated, it is clear that the extensions of the trajectories cross the eastern edge of the flare-loop arcade. The projected distance from that ranged from ~140'' for the 432.0 MHz source at the start of the rectilinear motion, to ~300'' for the 327.0 MHz source at the end, which gives an indication of the height. We note that the position

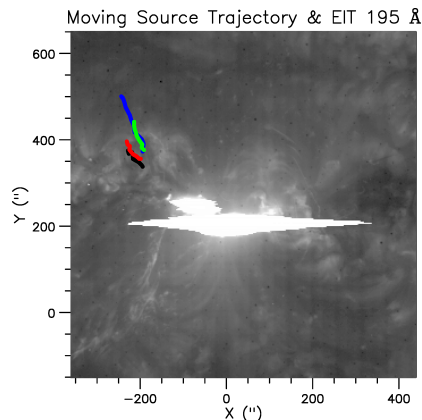


Fig. 3. Trajectories of the moving source at 432.0 MHz (black), 410.5 MHz (red), 327.0 MHz (green), and 236.6 MHz (blue) on top of an EIT 195 Å image at 10:36:10 UT. At 432.0, 410.5, and 327.0 MHz the trajectories are from 10:33:15 to 10:36:45 UT and at 236.6 MHz they are from 10:33:15 to 10:39:15 UT.

and the direction of motion at 432.0 MHz and 410.5 MHz were slightly different from those in the other two frequencies, which might indicate that we see two different magnetic structures.

The apparent velocity on the plane of the sky ranged from 200 km s⁻¹ at 432.0 MHz to 300 km s⁻¹ at 236.6 MHz, and therefore the distance of the 432.0 MHz source from the 236.6 MHz source increased with time. On the other hand, the relative frequency drift, measured from the delay of the bulk of the emission among the four highest NRH frequencies, was $-3.1 \times 10^{-3} \text{ s}^{-1}$; for a hydrostatic isothermal corona at $1.4 \times 10^6 \text{ K}$ and a height of 100 Mm above the photosphere, this drift corresponds to a radial speed of 500 km s⁻¹; to make this value compatible with the apparent speed requires an inclination of ~30° of the radial direction with respect to the sky plane.

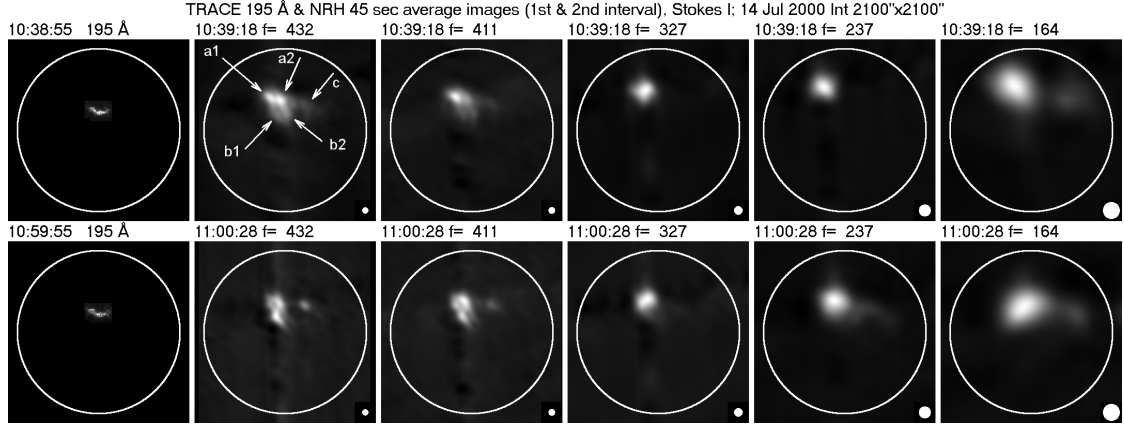


Fig. 4. Average NRH images in total intensity (Stokes I) during the first (*top*) and the second (*bottom*) interval, together with the corresponding TRACE images in the 195 Å band (*left column*). For the NRH images we used a circular clean beam in order to enhance some features. All images are normalized to their peak intensity.

Table 1. Average brightness temperature and polarization of NRH sources during the two selected intervals.

Freq. (MHz)	T_b , (10^8 K)				p , (%)			
	<i>a1</i>	<i>a2</i>	<i>b2</i>	<i>c</i>	<i>a1</i>	<i>a2</i>	<i>b2</i>	<i>c</i>
Interval 1								
164.0	5.3	–	–	–	20	–	–	–
236.6	32.5	–	–	–	50	–	–	–
327.0	11.0	–	–	–	50	–	–	–
410.5	4.9	2.9	1.4	0.8	85	64	28	–
432.0	2.3	2.4	1.0	0.6	62	61	40	–
Interval 2								
164.0	2.8	–	–	–	71	–	–	–
236.6	2.5	–	–	–	71	–	–	–
327.0	4.0	–	–	–	66	–	–	–
410.5	2.4	3.2	1.4	0.9	20	72	28	–85
432.0	1.7	2.6	2.9	1.4	20	75	80	–98

From the above description we conclude that the fiber bursts first appeared in a moving type-IV source, which developed after the primary energy release. We note that this moving type-IV source is not the same as the one described by Klein et al. (2001), which occurred earlier in the NW quadrant of the disk. The appearance of the fibers was probably associated with the rapid expansion of the flare ribbons and the formation of post-flare loops in the eastern part of the flaring region, while an association with the eastern footpoint of the CME flux rope is possible.

3.3. Structure of the fiber-emitting sources

Average NRH images during the two selected intervals of spike activity are shown in Fig. 4, together with the corresponding TRACE images at 195 Å. We used the full disk EIT images to compute the pointing of the TRACE images, which should be accurate to a few arc seconds. As for the NRH, the absence of image jitter (see next section) shows that the pointing is stable, whereas absolute pointing offsets due to ionospheric refraction are expected to be small during the summer.

During the first interval, the 432.0 and 327.0 MHz emission was dominated by two sources, marked *a1* and *a2* in the figure. These sources were located at the tip of two parallel, low-intensity stripes (*b1* and *b2* in the figure) extending to the SW; there was also a weak source, *c* in the west. Although there is

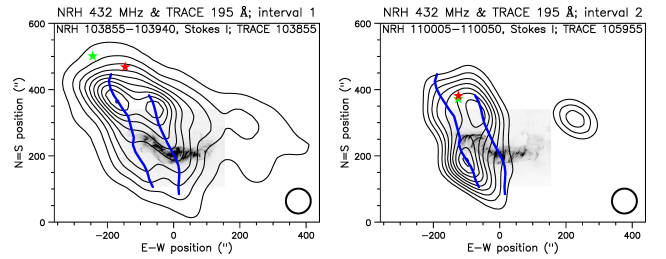


Fig. 5. Contours of the average NRH images at 432 MHz during interval 1 (*left*) and interval 2 (*right*) superposed on top of the corresponding (negative) 195 Å TRACE images. The blue lines mark the position of the two stripes during the first interval. The red and green stars mark the position of the 327.0 and 237.0 MHz peaks, respectively. The NRH beam is plotted in the lower right corner.

considerable structural change between the two intervals (see Movie 1), the same sources are detectable during the second interval. At 327.0 MHz, sources *a1* and *a2* merge and the stripes are not detectable, while source *c* is hardly visible. The convolution of the high-frequency images with the 327.0 MHz beam showed that these changes are real structural changes, rather than spatial-resolution effects.

The peak observed brightness temperature, T_b , and the degree of circular polarization, p , of sources *a1*, *a2*, *b2*, and *c* are given in Table 1. The radio sources are resolved, however their true size might be smaller than that observed (and hence their T_b higher), due to scattering of the radiation in the corona. In Interval 1 the observed T_b was much higher at 327.0 and 236.6 MHz than at other frequencies, reflecting the fact that these frequencies were near the peak of the drifting continuum discussed above (Fig. 1).

All bright sources were strongly polarized, that is, by 50% or more, at all frequencies with the exception of 164 MHz in Interval 1; it therefore appears that the emission at this frequency, which is well outside the drifting continuum, is part of a different structure. With the exception of source *c* during Interval 2, the polarization is in the right circular sense which, for o-mode emission, corresponds to magnetic polarity south of the neutral line.

The relative positions of the metric and EUV emissions are shown in more detail in Fig. 5. Here the EUV loop arcade serves in marking the neutral line of the magnetic field. In the same figure we have plotted the positions of the stripes, measured on

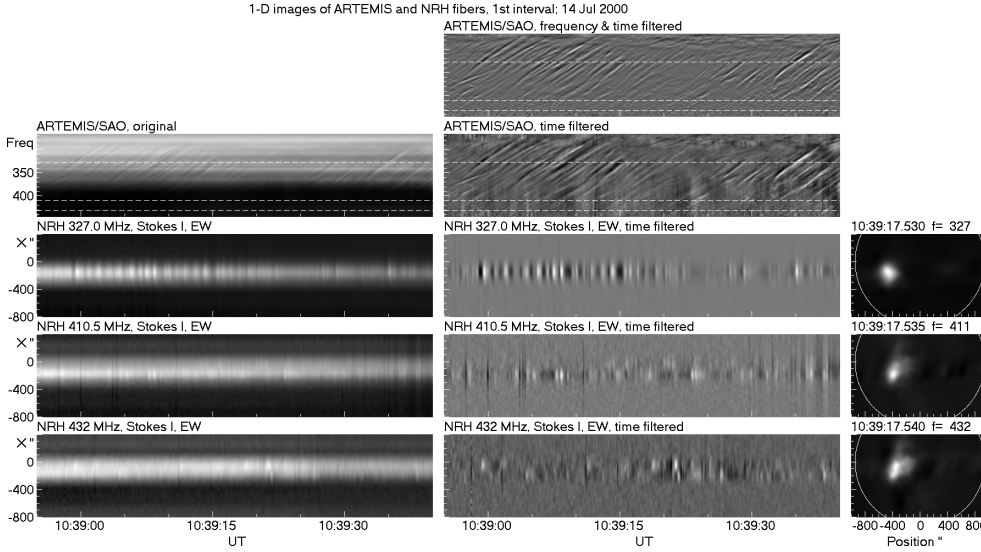


Fig. 6. *Left column:* original SAO dynamic spectrum and 1D Nançay EW images (scans) as a function of time for Interval 1. *Middle:* corresponding filtered images; in the *top row* the dynamic spectrum has been filtered in both time and frequency, in the others in time only. *Right:* average NRH images with the same orientation as the 1D images (west limb up). Dashed horizontal lines in the spectra mark the NRH frequencies.

the 432.0 MHz image during the first interval (blue lines). The distance between the stripes was about $100''$, which is about half of the EW extent of the loop arcade.

The two stripes appear to define segments of large-scale loops, with projected length of about 300 Mm, located above the post-flare loops. It is therefore certain that the continuum source and the fibers were not associated to the 195 \AA post-flare loops, but to a much larger magnetic structure. The comparison of the orientation of the large-scale loops with that of the post-flare loops shows that the former are inclined eastwards with respect to the latter; the same conclusion is drawn from the comparison with the model loops computed by Yan et al. (2001).

During the first interval, sources *a1* and *a2* together extended in longitude as much as the 195 \AA loop arcade, and are shifted with respect to that on the plane of the sky by $\Delta x = -60''$, $\Delta y = 100''$ (total $\sim 120''$). This shift is not compatible with a radial displacement of sources *a1* and *a2* with respect to the flare and strengthens the view expressed in the previous paragraph that the magnetic structure is inclined eastwards.

For Interval 2, we note that source *a1* is weak and *b2* even weaker than during Interval 1 and the emission is dominated by sources *b1* and *a2*, whose projected positions span the neutral line. At first sight, this might suggest that they are located near the legs of a magnetic loop; however, as shown in Fig. 5, *b1* is part of the east stripe and *a2* is part of the west stripe. This is corroborated by the fact that they are both polarized in the same sense, which indicates that they are both located in regions of the same magnetic polarity.

Source *c* is clearly visible during Interval 2 and is the only one with left-hand circular polarization. It is located at some distance from the west end of the flaring loop arcade, at the extension of the neutral line. We could not find any association of this source with magnetic or EUV features. During the first interval, source *c* is not well resolved. It appears to connect with source *a2* (see frame at 10:39:45, Movie 1) and its polarization was too low to be measured. We note that a very strong source existed earlier in the event, between 10:29 and 10:33 UT, at the same location as source *c* (see Movie 1), but its relation with source *c* is not clear.

3.4. Imaging of individual fibers

The most convenient way to visualize fine structures present in the NRH images is to compute 1D images (scans) and compare

them with the dynamic spectrum, as in Bouratzis et al. (2016). For this purpose the SAO data were integrated over 0.06 s in order to approach the NRH time resolution of 0.125 s; they were also subjected to a high-pass Gaussian filter of 5 s in width in the time domain and a high-pass Gaussian frequency filter of 20 MHz in width in order to suppress large-scale structures (Bouratzis et al. 2016). Furthermore, the filtered dynamic spectra were normalized by dividing the intensity of each frequency channel by its rms value. The 1D NRH scans were subjected to the same time filter but could not be subjected to frequency filtering. Shorter time filters gave similar results down to filter widths of ~ 1 s, which is close to the duration of the absorption-emission fiber pair.

Figure 6 shows the original and time-filtered 1D NRH intensity as a function of time for the first interval, with the 1D images computed in the EW direction; in the same figure we give the SAO dynamic spectrum (original, filtered in frequency and time, and filtered in time only), as well as the averaged NRH 2D images for reference. We first note that although fibers are hard to see in the original spectrum, they are readily visible in the filtered spectra. A similar improvement is noticed when comparing the time-filtered NRH 1D images to the original ones. We further note that in the dynamic spectra filtered in time only, broadband emissions do not significantly affect the fibers; we expect that the same is true for the 1D filtered images.

In spite of the lower time resolution of the NRH, practically all fiber bursts in the SAO spectra are detectable in the NRH 1D scans. These bursts appear as short-duration enhancements above the slowly varying background rather than as discrete sources, which was the case with spikes (cf. Fig. 16 of Bouratzis et al. 2016). In this interval, fibers are most easily visible at 327.0 MHz, being rather weak but still discernible at the higher frequencies. None of the 327.0 MHz fibers crossed the higher NRH frequencies; there are however a few fibers crossing both the 410.5 and 432.0 MHz levels.

The shape and position of fibers are best compared with the background source in 2D time-filtered images, which were computed by applying the high-pass time filter to each pixel of the original image set. Figure 7 gives a frame of the associated Movie 2, which shows all 2D NRH images in Interval 1, original and time-filtered, in Stokes *I* and *V*. In the frame shown in the figure we have a fiber in absorption at 327.0 MHz, no fiber at 410.5 MHz, and a fiber in emission at 432.0 MHz. Despite the

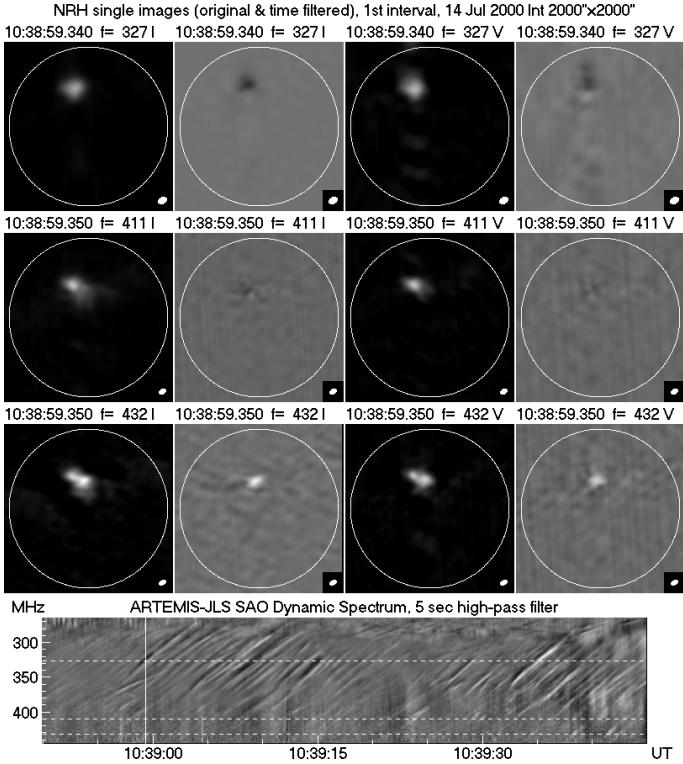


Fig. 7. Frame from [Movie 2](#), which shows the full sequence of 125 ms NRH images during Interval 1 at 327.0, (*first row* from the top), 410.5 (*second row*), and 432.0 MHz (*third row*). Each row shows the original and time-filtered images in Stokes I and V ; right-hand circular polarization is white. A linear gray-scale color table was used for the displays, where black corresponds to the minimum and white to the maximum intensity during the entire interval of each image set. At the bottom we show the time-filtered SAO spectrum, extended by 5 s on either side; the vertical line marks the time of the images and the dashed horizontal lines the NRH frequencies.

short integration of the individual NRH images, their quality is good, with a noise level of about 3×10^6 K, both in the original and the time-filtered images; we have only a few poor-quality images, which appear as vertical dark streaks in the 1D images of [Fig. 6](#).

[Figure 8](#) shows a selection of fiber images from Interval 1 at the three NRH frequencies, together with 45 s averaged images (left column). Only total-intensity images are given since the sources are uniformly polarized, but both I and V images are included in [Movie 2](#). At 432.0 MHz (bottom row in [Fig. 8](#)), the emission comes from the western source ($a2$) at 10:38:59.350 and 10:39:21.350 UT, from the eastern source ($a1$) at 10:39:26.480 UT, and from both sources $a1$ and $b2$ at 10:39:38.230 UT. These differences in position are also visible in the 1D scans of [Fig. 6](#). Similarly, at 410.5 MHz, source $a1$ alone is implicated at 10:38:30.600 and 10:39:43.970 UT, both $a1$ and $a2$ at 10:39:36.850 UT, and mostly source $a2$ at 10:39:42.850 UT. At 327.0 MHz (top row), the size and position of the fiber emission is very close to those of the single continuum source.

One-dimensional NRH scans for the second interval, this time along the NS direction, are given in [Fig. 9](#). Here fibers are also clearly visible both in the time-filtered dynamic spectrum and the time-filtered 1D scans; they are stronger at the NRH frequencies above 327.0 MHz, which is apparently a consequence of the fact that the continuum source moved to lower heights,

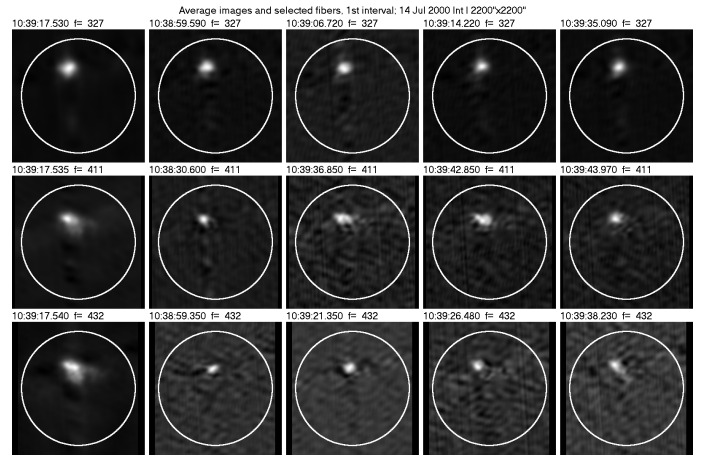


Fig. 8. Selection of time-filtered NRH images in Stokes I during Interval 1 at 327.0 (*top row*), 410.5 (*middle*) and 432.0 MHz (*bottom*). The average image at each frequency is shown in the left column for reference.

as mentioned previously ([Sect. 3.2](#)). Many fibers cross both the 432.0 and 410.5 MHz frequency levels, but hardly any cross all three. The full evolution is given in [Movie 3](#), a frame of which is shown in [Fig. 10](#), with fibers in absorption at 327.0 MHz and 432.0 MHz and in emission at 410.5 MHz.

It is obvious in the 1D scans of [Fig. 9](#) that in most cases the fiber emission extended over both sources $a1$ - $a2$ and $b1$ - $b2$. This is better shown in the selected images of [Fig. 11](#), where we have cases of fibers from sources $a1$, $a2$, and $b1$, as well as cases of emission from a single continuum source in between.

We note that source c showed occasional fiber activity, as in the 432.0 MHz image at 11:00:25.840 UT ([Fig. 11](#)); moreover, in one case (10:59:45.840 UT at 432.0 MHz, also in [Fig. 11](#)) there appears to be a connection between source c and the others. Taking this into consideration, as well as its polarization, source c might represent the other foot point of the large-scale loops. Apart from this occasional activity, source c was very stable both in intensity and in position and did not show up in most of the time-filtered 2D images ([Movie 3](#)); this shows, among other things, that our data are free of jitter due to refraction in the terrestrial atmosphere and ionosphere, at least for time scales shorter than the 5 s width of the applied filter.

The time sequences of 1D NRH images are convenient for checking fluctuations in circular polarization. Time variations in Stokes parameter V closely follow those in total intensity. Fluctuations in the degree of circular polarization are considerably weaker than fluctuations in I or V and, in general, in phase with them. Thus the degree of polarization of fibers in absorption is a few percent smaller than that of fibers in emission, a difference which we do not consider significant.

3.5. Apparent motions in individual fibers

In many cases, fibers in the 1D intensity-time displays ([Figs. 6](#) and [9](#)) are in the form of vertical streaks, which implies that the emission appears simultaneously over the entire structure. There are however cases where the fiber signatures are inclined, indicating apparent motions of individual features on the sky plane. One example is near 11:00:32 UT in the NS cuts of [Fig. 9](#); similar inclinations were detected in the EW cuts of the same fibers (not shown here). The inclinations suggest apparent motions from west to east and from south to north, that is, from the lower

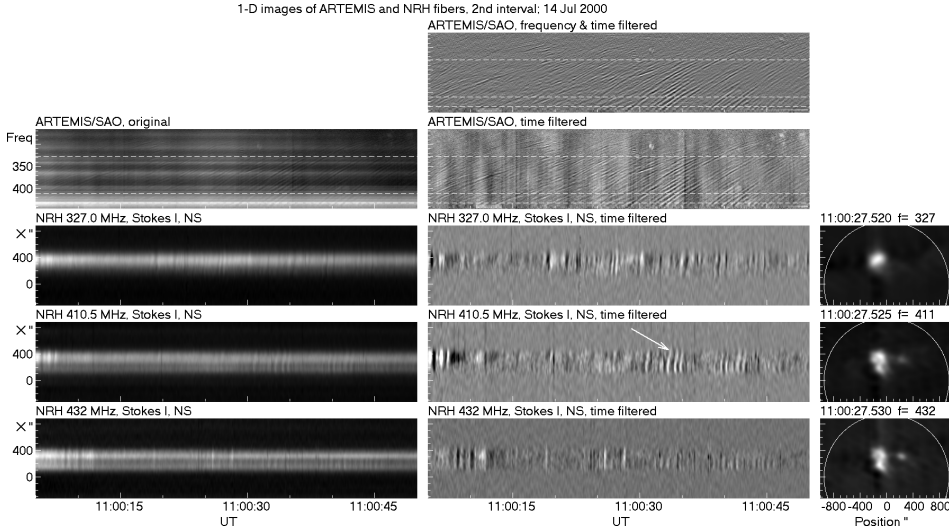


Fig. 9. Same as Fig. 6 but for the second interval, with the 1D scans in the NS direction. The arrow marks fibers exhibiting apparent motion. The average images on the right are oriented with north in upward direction.

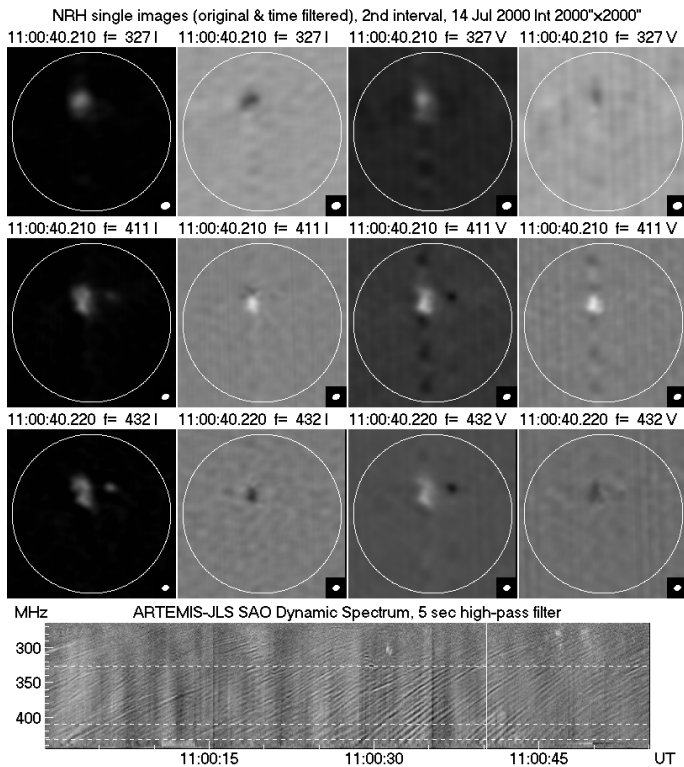


Fig. 10. Same as Fig. 7, but showing a frame from Movie 3 (Interval 2).

to the upper part of the loops associated with the two stripes. The apparent velocity, measured by 2D autocorrelation, is supra-luminal, ranging from $4c$ to $10c$.

In Fig. 12 we present sequences of five filtered 2D images (500 ms) of four fibers at 432.0 MHz. The fiber at around 11:00:05 UT (first row below the average image) was practically stationary, while the other three showed clear apparent motions from SW to NE, in conformity with the results from the 1D image analysis. We first note that in some of the images shown in this figure, as well as in many others, fibers in absorption coexist with fibers in emission. Thus in the first image of the bottom row we have absorption at the location of source $b1$. In the next frame this absorption shrinks and we have new absorption at the location of sources $a1$ and $a2$, and one image later $b1$ appears in

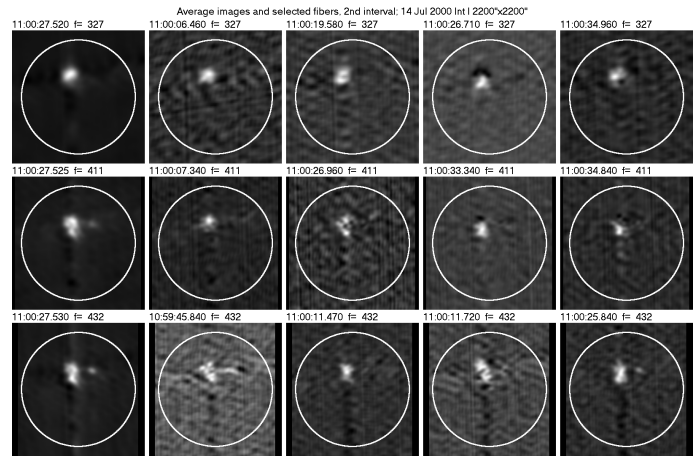


Fig. 11. Selection of time-filtered NRH images in Stokes I during Interval 2. The average image at each frequency is shown in the left column for reference.

emission. In the fourth image the emission at $b1$ disappears and we have emission from source $a1$, while in the last image we have new absorption at the location of source $b1$. Similar is the situation with the time sequences starting at 11:00:34.59 and at 11:00:33.09 UT, except that in these we also have emission from source $a2$ in the fourth frame.

We conclude that what in the dynamic spectrum appears as a single fiber is actually a complex of multiple wave trains that cross the plasma level at slightly different times and positions, giving the impression of an apparent motion which may exhibit supra-luminal velocity. Figure 12 indicates that the duration of each train is comparable to the time difference between successive trains, which explains why such trains do not appear as separate fibers in the dynamic spectrum. It is however rather peculiar that the pattern of trains repeats itself several times, as indicated by the similarity of the time evolution of the three fibers of Fig. 12.

3.6. Fiber images at two frequencies

The best observed cases of fibers crossing two NRH frequencies were during the second interval and for the closely spaced frequencies of 432.0 MHz and 410.5 MHz. In Fig. 13 we give

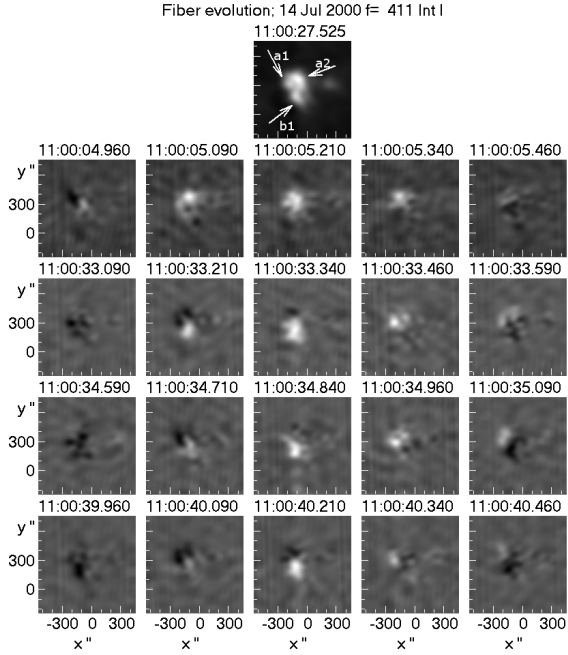


Fig. 12. Time sequences of filtered NRH 2D images, showing the evolution of four fibers at 410.5 MHz during the second interval. These images were taken at intervals of 125 ms. We give the corresponding average image in the *top row* for reference.

sequences of five images at 432.0 MHz of the same fibers that are shown in Fig. 12. The time delay between the two frequencies is 2.75 s for the first fiber and 1.5 s for the other three, corresponding to frequency drifts of -7.8 and -14.3 MHz s^{-1} , respectively.

Although the images of the same fiber at the two frequencies are similar, they are not identical. Differences could be attributed to the fact that the actual time delay is not an integer multiple of the image cadence, therefore evolution effects including the apparent motions discussed in the previous section play a role in the form of the radio sources. For the same reasons, the (small) differences in the position of individual fibers between 432.0 and 410.5 MHz cannot be accurately measured.

3.7. Exciter speed and frequency scale length

Although, as mentioned previously, we cannot identify any fibers that cross all three NRH frequencies, from 11:00:29 to 11:00:45 (second interval) we see a pattern of fibers that varies smoothly between 432.0 MHz and 327.0 MHz (Fig. 10). Using the method of cross correlation with a sliding spectral window described in Sect. 2.2.2 of Paper I, we computed the average track of this group of fibers on the dynamic spectrum, and from that we obtained time delays of 1.74 and 8.52 s for 410.5 MHz and 327.0 MHz, with respect to 432.0 MHz.

We also measured the position shift, considering that the average 2D images, taking into account the time delays, closely represent the position of the fiber sources. By convolving these images with the 327.0 MHz beam and measuring the source positions through a least-square fit of sources *a1* and *a2* together with a single Gaussian, we obtained shifts of $18''$ and $58''$ for 410.5 MHz and 327.0 MHz, with respect to 432.0 MHz. From these measurements, we computed the speed of the exciter on the plane of the sky and found a value of 5 Mm s^{-1} , in good agreement with the results of Paper I (Fig. 17, left histogram), computed from the frequency drift rate.

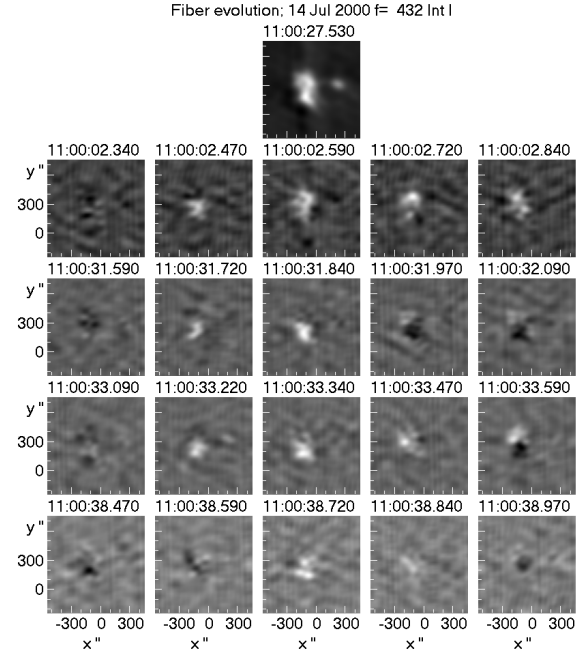


Fig. 13. Same as Fig. 12 but for 432.0 MHz.

From the position shifts and the corresponding frequencies we also computed the frequency scale length (twice the density scale length) along the loop, projected on the plane of the sky, ℓ_f . For an isothermal loop, the plasma frequency varies with distance, x , along the loop as:

$$f = f_0 \exp\left(-\frac{x - x_0}{\ell_f}\right). \quad (1)$$

We obtained a value of $\ell_f = 146$ Mm. On the other hand, the value of the frequency scale length along the loop, $h_f = H_f / \cos \theta$, where H_f is the scale in the radial direction and θ the angle between the loop segment and the vertical, can be computed by fitting the average fiber track to the expression in Eq. (11) of Paper I. This expression was derived for a simple model of the fiber tracks on the dynamic spectrum; it is independent of coronal parameters, but presumes a whistler origin of the emission. We obtained $h_f = 183$ Mm.

The quantities ℓ_f and h_f are related through the simple expression

$$\ell_f = h_f \cos \beta, \quad (2)$$

where β is the angle between the line of sight and the loop segment, and the above measurements give $\beta = 37^\circ$. For a simple geometrical model of a vertical semicircular loop, we have

$$\beta = 90^\circ - \alpha - \theta, \quad (3)$$

where α is the angle between the line of site and the radial direction and θ is as defined above. Taking $\alpha \sim 16^\circ$ (equal to the flare latitude), we get $\theta \sim 37^\circ$, which places the fiber-emitting sources *a1* and *a2* above the middle of the leg of the large-scale loop.

Thus, the 2D images and dynamic spectrum give consistent results both for the exciter velocity and for the frequency scale length. Moreover, we have one more element in favor of whistler origin of fibers, since the analysis of spectral data that we used to measure the frequency scale was based on that assumption.

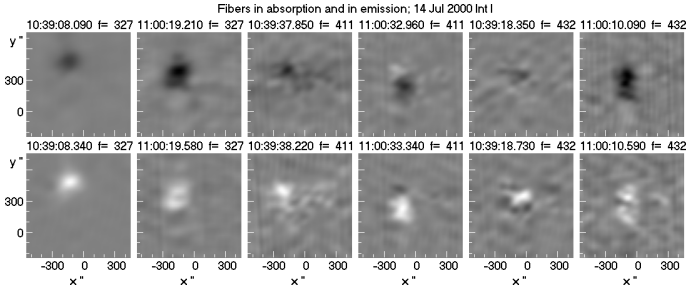


Fig. 14. Time-filtered images of fibers in absorption (*top row*) and in emission (*bottom*). One case is shown for each interval and each NRH frequency. Each pair of fiber images is normalized to the same minimum and maximum values.

3.8. Fibers in emission and absorption

According to the theory of whistler origin (cf. Sect. 1), the fiber emission appears at $f_{pe} + f_w$ and the absorption at f_{pe} . Thus, at a fixed frequency the absorption will precede the emission by

$$\Delta t = -f_w \left(\frac{df}{dt} \right)^{-1}, \quad (4)$$

where df/dt is the frequency drift rate. The whistler frequency is equal to the frequency difference of the absorption and emission ridges, and therefore Δt can be computed from the dynamic spectrum; it amounts to 350 ms for Interval 1 and 250 ms for Interval 2.

Figure 14 shows some examples of fiber pairs in absorption and in emission; two pairs are presented for each frequency, all from Interval 1. The time difference is from 250 ms to 500 ms (2–4 NRH images), in conformity with the prediction of the previous paragraph. We note that the shape and size of the absorption and emission of each fiber pair are very similar, which verifies the hypothesis that they are manifestations of the same wave train. The difference in their intensities from the background are similar, although exact measurements are uncertain, as the intensity values might be affected by the filtering process. Their position is also very close, but it cannot be measured with certainty due to the apparent motions that some fibers exhibit (Sect. 3.5).

4. Summary, discussion, and conclusions

The combined spectral and imaging observations with ARTEMIS-JLS/SAO and the NRH reveal a number of important aspects of fiber bursts observed during the flare event of July 14, 2000, which we summarize and discuss in this section.

We find that the fibers modulate the intensity of the radio emission by about 10%, below the 30 to 40% range reported by Wang et al. (2017) at higher frequencies. Therefore, images averaged over several seconds are representative of the background emission. We used such images to study the evolution of the continuum and its association with the fibers.

The first fibers were detected in a moving type-IV source, which in the dynamic spectrum manifested itself as a broadband drifting continuum that started after the GOES and HXR peaks. This emission occurred NE of the flare and was probably associated to the rapid eastward expansion of the flare and the associated loop arcade that formed at about the same time; that was after the main energy release and the filament activation, which occurred in the western part of the active region. The fibers appeared near the peak intensity of the drifting continuum and close to the time that the radio sources started an upward

rectilinear motion with a projected velocity of 200–300 km s⁻¹ that lasted for 4–6 min. After this upward motion, the continuum source moved in an irregular way to the SE, approaching the eastern part of the post-flare loop arcade. This downward motion could be the result of the decrease with time of the ambient electron density in the associated magnetic structures, that causes the plasma level corresponding to the observing frequencies to move to lower heights.

We selected two 45 s intervals that were not contaminated by pulsations and other broadband structures for further study. Average images representing the background continuum revealed two parallel stripes, *b1* (east) and *b2* (west), apparently segments of large-scale loops, much larger than the EUV post flare loops and inclined eastward with respect to the latter. This indicates that the plasma that produced the type-IV source and the fiber emission was confined in such loops and was not associated with the post-flare loops seen in the EUV. We note that Aurass et al. (2005) found that the lines of force of their extrapolated magnetic field were higher than the soft X-ray flare loops. A similar conclusion is drawn from Fig. 7a of Rausche et al. (2007). On the other hand, Wang et al. (2017) reported that the fiber sources around 1400 MHz were near and above one foot-point of the flare loops; this might be due to the fact that their observing frequency was considerably higher than that of the NRH, hence plasma emission should originate from a higher-density region located lower in the fiber loop.

The fact that all sources implicated in the fiber emission were polarized in the same sense supports the geometry suggested above. The observed polarization was right handed, in the sense of the ordinary mode south of the neutral line. The mere presence of fiber bursts indicates plasma emission and the strong polarization points to emission at the fundamental, which is expected to be highly polarized in the ordinary sense because the extraordinary mode is evanescent near this frequency.

The whistlers are excited as a result of a loss-cone instability (Kuijpers 1972), the development of which depends on the value of the loss-cone aperture angle. In the case of an asymmetric loop, it is possible that the instability will develop in one leg of the loop as, according to Aurass et al. (2005), conditions are more favorable at the weak field footpoint. This probably explains why we do not see emission from both legs of the large-scale loops.

A possible explanation of the large size of the stripes in comparison to the EUV loops is that they are portions of large-scale loops encompassing both the CME-associated flux rope and the EUV flare loops (see, e.g., Fig. 1 of Reeves & Forbes 2005). Their location near the east end of the flux rope may explain their large inclination, as the flux rope expands more rapidly in the middle, pushing these loops eastwards.

The projected length of the stripes was about 300 Mm. Assuming a semi-circular loop, a hydrostatic density model with a temperature of 1.5×10^6 K and a base density four times that of the Newkirk model (Sect. 5.4 of Paper I), we obtained from the fiber tracks in the dynamic spectrum a radius very close to the measured projected length.

In order to facilitate the comparison of the fiber signatures in the images and the dynamic spectrum at full NRH time resolution, we applied a Gaussian high-pass filter of 5 s in width in the time domain to suppress slowly varying emissions; for the dynamic spectra, we also applied a Gaussian high-pass filter of 20 MHz in width in the frequency domain to suppress broadband features. Furthermore, for the three NRH frequencies that were inside the SAO band (327.0, 410.5 and 432.0 MHz), we computed both 2D images from the original visibilities and 1D images by integration of the 2D images in the EW and NS

directions. This processing made the fibers very prominent both in the dynamic spectra and in the sequence of images.

Practically all fibers visible in the SAO dynamic spectra are detectable in the NRH 1D scans and 2D images. We found that some fibers originated in stripe *b1* and the associated source *a1*, some in *b2* and source *a2*, and some in between, indicating interactions between the associated loops. We found very small changes of the degree of circular polarization associated with fibers.

A close examination of the 2D time-filtered images revealed cases of multiple-fiber emissions appearing at slightly different positions and times. The time differences are comparable to the duration of the emission, and therefore they appear as single fibers in the dynamic spectrum. The consecutive appearance of such emissions gives the impression of apparent motion with supra-luminal velocities.

Although we found no fibers crossing all three NRH frequencies that were inside the SAO frequency range, we had a number of fibers crossing the closely spaced frequencies of 432.0 and 410.5 MHz. Their images were very similar, but we could not reliably measure position differences. Position shifts and the corresponding time delays between 327.0 and 432.0 MHz were measured for a group of fibers that varied smoothly between the two frequencies; our measurements led to estimates of the exciter speed and the frequency scale length, with spectral and imaging data giving consistent results, supporting the hypothesis of a whistler origin for the fibers. We also found that the upper sources *a1* and *a2* were located above the middle of the leg of the large-scale loop.

Finally, we examined fibers appearing in absorption. We found that the shape and size of the absorption and emission fibers are very similar, which verifies the hypothesis that they are manifestations of the same wave train.

This study confirms the importance of simultaneous spectral and imaging observations of the metric radio emissions. Our analysis revealed the geometry of the continuum and the fiber sources, made it possible to directly measure the exciter speed and frequency scale length, revealed multiple wave trains unresolved in the dynamic spectrum, and provided concrete evidence that fibers in emission and absorption are indeed produced by the same wave train. Moreover, we found that the whistler hypothesis we adopted works well with the imaging results, confirming our conclusion in Paper I, based on spectral data. Future work could include nonlinear magnetic field extrapolations, as well as the analysis of a larger sample of events to verify the conclusions reached in this work.

Acknowledgements. We wish to thank our colleagues from the Observatoire de Paris-Meudon and the NRH staff for providing the original visibility data. The authors are grateful to the other members of the ARTEMIS group, C. Caroubalos, P. Preka-Papadema, X. Moussas, A. Kontogeorgos and P. Tsitsipis, for their support work. We also wish to thank A. Nindos and S. Patsourakos for useful discussions and comments. Data from TRACE, GOES, the RSTN network, MTI/HXRS and HXT were obtained from the respective data bases; we are grateful to all those who contributed to the operation of these instruments and made the data available to the community.

References

- Aurass, H., Rausche, G., Mann, G., & Hofmann, A. 2005, *A&A*, **435**, 1137
 Bouratzis, C., Hillaris, A., Alissandrakis, C. E., et al. 2015, *Sol. Phys.*, **290**, 219
 Bouratzis, C., Hillaris, A., Alissandrakis, C. E., et al. 2016, *A&A*, **586**, A29
 Bouratzis, C., Hillaris, A., Alissandrakis, C. E., et al. 2019, *A&A*, **625**, A58 (Paper I)
 Caroubalos, C., Maroulis, D., Patavalis, N., et al. 2001a, *Exp. Astron.*, **11**, 23
 Caroubalos, C., Alissandrakis, C. E., Hillaris, A., et al. 2001b, *Sol. Phys.*, **204**, 165
 Elgarøy, 1972, in *CESRA-3, Committee of European Solar Radio Astronomers*, eds. J. Delannoy, & F. Poumeyrol, 3, 174
 Benz, A. O., & Mann, G. 1998, *A&A*, **333**, 1034
 Bernold, T. E. X., & Treumann, R. A. 1983, *ApJ*, **264**, 677
 Fomichev, V. V., & Chertok, I. M. 1978, *Radiofizika*, **20**, 1255
 Kerdraon, A., & Delouis, J. M. 1997, in *Coronal Physics from Radio and Space Observations*, ed. G. Trotter (Berlin: Springer Verlag), Lecture Notes in Physics, 483, 192
 Karlický, M., Mészárosová, H., & Jelínek, P. 2013, *A&A*, **550**, A1
 Klein, K.-L., Trotter, G., Lantos, P., & Delaboudinière, J.-P. 2001, *A&A*, **373**, 1073
 Kuijpers, J. 1972, in *CESRA-3, Committee of European Solar Radio Astronomers*, eds. J. Delannoy, & F. Poumeyrol, 3, 130
 Kuijpers, J. 1975, *Sol. Phys.*, **44**, 173
 Kuijpers, J. 1980, in *Radio Physics of the Sun*, eds. M. R. Kundu, & T. E. Gergely, *IAU Symp.*, **86**, 341
 Kuznetsov, A. A. 2006, *Sol. Phys.*, **237**, 153
 Masuda, S., Kosugi, T., & Hudson, H. S. 2001, *Sol. Phys.*, **204**, 55
 Reeves, K. K., & Forbes, T. G. 2005, *ApJ*, **630**, 1133
 Rausche, G., Aurass, H., Mann, G., Karlický, M., & Vocks, C. 2007, *Sol. Phys.*, **245**, 327
 Rausche, G., Aurass, H., & Mann, G. 2008, *Cent. Eur. Astrophys. Bull.*, **32**, 43
 Slotje, C. 1972, *Sol. Phys.*, **25**, 210
 Slotje, C. 1981, *Atlas of Fine Structures of Dynamic Spectra of Solar Type IV-dm and Some Type II Radio Bursts*, Dissertation, N.F.R.A Dwingeloo and Astronomical Institute of Utrecht
 Wang, S., Yan, Y., Zhao, R., et al. 2001, *Sol. Phys.*, **204**, 153
 Wang, Z., Chen, B., & Gary, D. E. 2017, *ApJ*, **848**, 77
 Yan, Y., Deng, Y., Karlický, M., et al. 2001, *ApJ*, **551**, L115
 Young, C. W., Spencer, C. L., Moreton, G. E., & Roberts, J. A. 1961, *ApJ*, **133**, 243
 Zlobec, P., & Karlický, M. 2014, *Sol. Phys.*, **289**, 1683